Correspondence to:

Y. Jiang,
jiangyh@whu.edu.cn

Author Contributions:

Conceptualization: D. Li, Y. Jiang
Data curation: S. Wei
Formal analysis: D. Li, J. Li, S. Wei, W. Liu
Investigation: G. Zhang
Methodology: D. Li, Y. Jiang, G. Zhang, S. Wei
Validation: D. Li, J. Li, W. Liu
Writing – original draft: D. Li
Writing – review & editing: Y. Jiang, W. Liu

Geometric Calibration of the ESA Mars Express Orbiter High Resolution Stereo Camera

D. Li[1] , **Y. Jiang[2]** , **J. Li[3], G. Zhang[1], S. Wei[1], and W. Liu[1]**

[1]State Key Laboratory of Information Engineering in Surveying, Mapping and Remote Sensing, Wuhan University, Wuhan, China, [2]School of Remote Sensing and Information Engineering, Wuhan University, Wuhan, China, [3]Wuhan GEOWEAY Space Information Technology Research Institute Co., Wuhan, China

Abstract The high-resolution stereo camera mounted on the Mars Express (MEX) spacecraft of the European Space Agency is specifically designed for planetary photogrammetry and mapping missions. High-precision geometric calibration is required to maintain the geometric quality of satellite imaging. This study aimed to develop a Martian geometric calibration model based on the detector look angle and offset matrix to compensate for systematic errors caused by the camera system parameters, Doppler shift measurements, and other parameters of the interior and exterior orientation during positioning. Moreover, the difficulty in identifying high-precision geometric ground control points from extra-terrestrial imagery was addressed by proposing an iterative Mars Orbiter Laser Altimeter extraction algorithm based on the similarity measure of terrain relief. Using this algorithm, constraint conditions were established, and a calibration model was introduced to achieve in-orbit geometric calibration of the MEX satellite. The proposed method is effective in reducing the distortion of the camera in calibration images from 12 pixels to <1 pixel, both before and after calibration. Moreover, the plane accuracy of validation images improved from approximately 900 to 200 m, while elevation accuracy improved from 500 to 100 m, verifying the effectiveness of the proposed method.

1. Introduction

In 2004, the Mars Express (MEX) spacecraft (Chicarro et al., 2004) launched by the European Space Agency began capturing images of Mars. The High Resolution Stereo Camera (HRSC; Neukum et al., 2004) aboard the spacecraft is specifically designed for planetary photogrammetry and mapping missions. The camera operates in a line-array pushbroom imaging mode, which enables the acquisition of high-resolution stereo images of the Martian surface in near real-time, thereby avoiding time-dependent changes in observational conditions. The probe orbits Mars along an elliptical trajectory and captures imagery at the nearest point to the orbit, at a height of approximately 250 km. The highest achievable resolution of the captured imagery is 10 m/pixel with a width of approximately 53 km. This level of imaging capability satisfies the requirements for tasks such as constructing three dimensional (3D) models of the Martian surface and producing color orthoimages, terrain maps, and thematic maps (Albertz et al., 2005; Scholten et al., 2005).

Prior to the satellite launch, the HRSC line sensors were geometrically calibrated based on extensive laboratory measurements to obtain the camera system parameters, as listed in Table 1. The HRSC camera can simultaneously acquire images in nine spectral bands, including five panchromatic bands and four multispectral bands (red, green, blue, and near-infrared). In addition to the nadir panchromatic band, the other four panchromatic bands are arranged at stereo angles of ±18.9° and ±12.8°, respectively. The camera has a focal length of 175 mm, a pixel size of 7 μm, and each charge coupled device (CCD) chip contains 5,272 detector elements, of which 5,184 are used for image acquisition. Owing to the limited transmission bandwidth, the images acquired in eight spectral bands other than the nadir band underwent varying degrees of compression. The camera was rigidly mounted to the spacecraft's attitude control system, and its installation relationship was strictly calibrated. However, the camera system parameters and installation status are subject to changes during in-orbit operation owing to the detector launch process and harsh space environment. Therefore, periodic in-orbit geometric calibration is required to mitigate the impact of system errors and ensure high-precision satellite mapping.

When performing satellite geometric calibration tasks, it is typically necessary to deploy ground targets or obtain high-resolution, high-precision digital ortho-images and digital elevation model products (Jiang, Zhang, Tang, Li, et al., 2013; Jiang, Zhang, Tang, & Zhu, 2013; Wang et al., 2017; Zhang et al., 2014) to obtain a sufficient number of high-precision GCPs in the experimental area. However, for extra-terrestrial exploration missions such

Table 1
Fundamental Parameters of HRSC (Calibration by Laboratory Prior to Satellite Launch)

Camera parameters	HRSC
Image principle	Multi-line pushbroom
Image size	5,184 pixels/line (9 CCD lines)
Sensor pixel size	7×7 μm
Focal length	175 mm
IFOV	8.2 arcsec
Along-track stereo angle	ND: 0°, P1/P2: ±12.8°, S1/S2: ±18.9°
Spectral bands	5 panchromatic, near-infrared, red, green, blue
On-board compression	Yes

as those to Mars, these conditions are typically difficult to satisfy, making it challenging to provide high-precision GCPs (Kim & Muller, 2007). Consequently, to enhance the geometric positioning accuracy of Mars orbiter images, a bundle block adjustment method based on the Mars Orbiter Laser Altimeter (MOLA) digital terrain model (DTM) product elevation constraint derived from MOLA data (Neumann et al., 2001; Smith et al., 1999, 2001) of the Mars Global Surveyor (MGS) spacecraft has been widely applied. To circumvent the identification of control points in the optimization process, previous studies pioneered the establishment of an adjustment model based on DTM constraints (Ebner & Müller, 1987; Ebner & Ohlhof, 1994; Ebner & Strunz, 1988) and validated the effectiveness of this method using simulation data. Spiegel (2007a, 2007b) adopted this constraint model and utilized the MOLA DTM as control data to successively optimize the image principal point coordinates, satellite orbit position, and attitude parameters of the MEX HRSC. They also applied the obtained calibration parameters (image principal point coordinates) to produce HRSC standard products in the Planetary Data System (PDS) (Hughes et al., 2014; Putri et al., 2019). Subsequently, Schmidt et al. (2008) further utilized tie points and elevation consistency constraints based on the aforementioned work, and conducted a two-step optimization of the satellite exterior orientation parameters to register the stereo image data set of 1,138 orbits to the MOLA global reference system. However, traditional geometric processing methods have three main drawbacks: (a) as the satellite operates in orbit for a long time, the other interior orientation elements of HRSC (e.g., camera focal length and sensor arrangement) besides the image principal point coordinates may also change; (b) the MOLA DTM product is produced by MOLA interpolation, which may result in accuracy loss compared with the original MOLA data, and the adjustment model following the prior condition that HRSC points must lie on the surface defined by MOLA DTM; (c) in order to register the stereo images to the MOLA global reference system, the orientation image method is used to calculate the exterior orientation parameters for each image line of each orbit stereo image, which may affect the efficiency of product production (Edmundson et al., 2012).

This study aimed to develop a geometric calibration model based on the detector look angle and offset matrix, which is mainly applied to process Earth's remote sensing images. This model was designed to compensate for the systematic errors introduced by the camera system parameters, Doppler shift measurements, and other parameters of the interior and exterior orientation in the positioning process. In addition, the calibration parameters can be directly added to the positioning models of other orbit images to improve the direct positioning accuracy of the cameras and the production efficiency of downstream products. In addition, to address the difficulty of accurately identifying the MOLA footprints in HRSC Stereo images, this study constructed a robust matching unit of a laser point set and realized the accurate alignment between MOLA data and stereo images according to the similarity measure of terrain relief consistency. This set of control data, compared with the traditional approach that uses the MOLA DTM, has the advantage of providing planar control and avoiding the error introduced by the DTM elevation constraint owing to planar positioning deviation. Additionally, direct processing of the original MOLA data can prevent accuracy loss introduced by the production of MOLA DTM products. Our experimental results show that using the discrete MGS MOLA precision experiment data record (PEDR) as a control reference for in-orbit geometric calibration of the MEX satellite improves horizontal accuracy from approximately 900 m to within 200 m and the elevation accuracy from 500 m to within 100 m, confirming the correctness and feasibility of the method proposed in this paper.
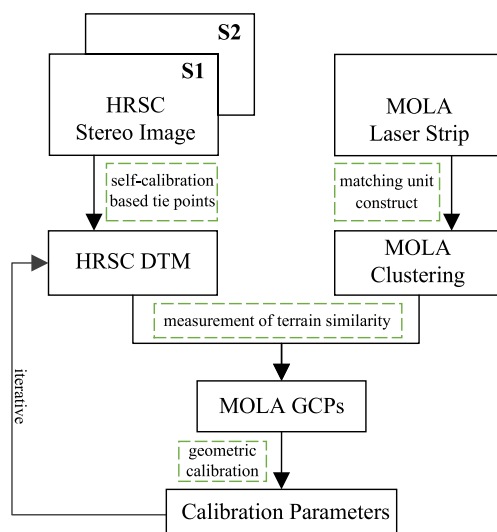
2. Materials and Methods

To improve the positioning accuracy of the HRSC, the method shown in Figure 1 was adopted to calibrate the internal and external orientation elements of the camera. The process involves several steps, including automatic image matching to obtain a sufficient number of evenly distributed tie
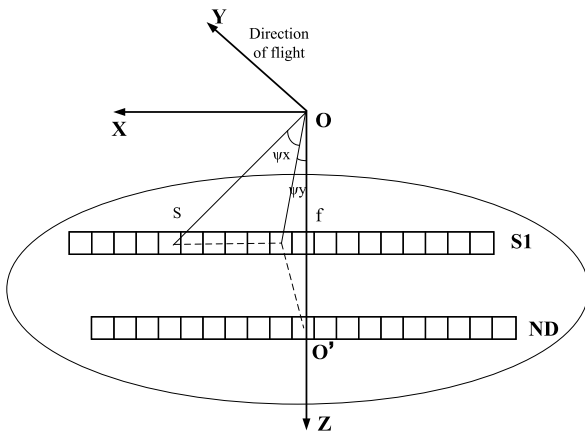

Figure 1. Framework of the high resolution stereo camera geometric calibration experiment.

Figure 2. High resolution stereo camera detector pointing angle model.

points to create a self-calibration model to ensure internal consistency and construct an HRSC DTM based on this model (Granshaw, 2020). Next, a matching-unit algorithm was used to process the laser strip to obtain robust matching units. The laser matching units were then compared with the local HRSC DTM for elevation similarity measurements, and the corresponding image control points were identified. Finally, the control points were adjusted using a geometric calibration model to produce the HRSC calibration parameters. It is worth noting that the entire calibration process requires multiple iterations of HRSC image control point production and geometric calibration until the positioning accuracy converges. Each iterative process involves two rounds of bundle adjustment: the first bundle adjustment occurs during the "self-calibration base tie points" phase, while the second bundle adjustment occurs in the "geometric calibration" phase. During the latter phase, an error correction model is established based on tie points and robust laser control points.

2.1. HRSC Geometric Calibration Model

The imaging data acquired by the camera on the accompanying satellite of the camera system adhered to the central projection imaging principle. This allows for the development of a rigorous geometric imaging model for the MEX–HRSC, which can be constructed as

$$\begin{bmatrix} X \\ Y \\ Z \end{bmatrix} = R_{J2000}^{\mathrm{Mars}} \begin{bmatrix} X_S \\ Y_S \\ Z_S \end{bmatrix} + m R_{J2000}^{\mathrm{Mars}} R_{\mathrm{MEX}}^{J2000} R_{\mathrm{CameraMEX}} \begin{bmatrix} X_C \\ Y_C \\ Z_C \end{bmatrix} \tag{1}$$

where transformation matrix $R_{J2000}^{\mathrm{Mars}}$ indicates the conversion between the $J2000$ inertial frame and the IAU-Mars fixed frame; $(X_S, Y_S, Z_S)^T$ indicates the position vector of the satellite center in the $J2000$ inertial frame; R_{MEX}^{J2000} represents the transformation matrix for the satellite center relative to the $J2000$ inertial frame, obtained from the attitude measurement device; $R_{\mathrm{CameraMEX}}$ represents the camera installation matrix, which was calibrated in the laboratory prior to satellite launch and released by the Navigation and Ancillary Information Facility (NAIF; Acton et al., 2016) with supporting information; $(X_C, Y_C, Z_C)^T$ denotes the position vector of the image point in the camera coordinate system; and m represents scales.

The geometric calibration model consists of two parts that calibrate the internal and external orientation elements of the camera during the imaging process. First, in the internal calibration model, the polynomial coefficients (shown in Equation 2) of the pointing angle model are optimized to compensate for errors such as the image principal point offset, principal distance error, detector size error, and lens optical distortion error. This process individually restores the true detector pointing direction in the camera coordinate system (as shown in Figure 2).

As shown in Figure 2, based on the laboratory calibration results of the camera's principal distance, sensor pixel size, and principal point position, the image point coordinates $(X_C, Y_C, Z_C)^T$ in the camera coordinate system were calculated for a rigorous geometric imaging model. These calculated values serve as the initial values for the polynomial coefficients in the pointing angle model,

$$\begin{aligned} \tan \psi_x &= \frac{X_C}{Z_C} = m_0 + m_1 s + m_2 s^2 + \dots \\ \tan \psi_y &= \frac{Y_C}{Z_C} = n_0 + n_1 s + n_2 s^2 + \dots \end{aligned} \tag{2}$$

where s represents the index of each CCD pixel in the camera and $(m_i, n_i)(i = 0,1,2\dots)$ indicates the polynomial coefficients in the pointing angle model.

Second, considering the impact of various errors, such as the satellite orbit, attitude measurement, and camera installation, the position deviation of the object point caused by the satellite orbit error during the satellite

Table 2
Measurement Errors of MEX Line Elements and Angular Elements (Spiegel, 2007b)

Item	X,Y,Z	φ,ω,κ
Bias	1,000 m	
Drift per line	0.01 m	
Orientation		25 mdeg

push-broom imaging process can be equivalent to the attitude error (i.e., both have the same effect on the geometric positioning accuracy). The offset matrix $R_u(\varphi,\omega,\kappa)$ is introduced in the external calibration model construction to compensate for the directional deviation between the actual light and the ideal light (Jiang, Zhang, Tang, & Zhu, 2013).

For Earth observation satellites, high-precision orbit determination can usually be achieved with centimeter-level positioning accuracy by completing precise orbit determination using GPS measurements. However, for the MEX, which uses Doppler shift measurements, its orbit determination accuracy can only be guaranteed to reach the kilometer level (Table 2). In addition, the attitude measurement of the MEX, which characterizes its spatial orientation using three angular elements, has accuracy values of 0.025° for all three rotation angles (Spiegel, 2007a). Moreover, the rigid connection between the camera sensor and attitude measurement system involves a relative positional relationship between multiple coordinate system references, such as the spacecraft, sensor, and camera references. This connection is also subject to new camera positioning errors introduced by other factors, such as illumination, temperature, and thermal deformation, during long-term operation.

The geometric calibration model was established by combining Formulas 1 and 2 while considering the measurement errors of both the interior and exterior orientation elements and eliminating the correlation effects among various parameters.

$$\begin{bmatrix} X \\ Y \\ Z \end{bmatrix} = R_{J2000}^{\text{Mars}} \begin{bmatrix} X_S \\ Y_S \\ Z_S \end{bmatrix} + m R_{J2000}^{\text{Mars}} R_{\text{MEX}}^{J2000} R_u R_{\text{Camera}} \begin{bmatrix} m_0 + m_1 s + m_2 s^2 \\ n_0 + n_1 s + n_2 s^2 \\ 1 \end{bmatrix} \tag{3}$$

2.2. HRSC Iterative Calibration Algorithm

2.2.1. Self-Alignment Algorithm Base of Tie Points

To ensure the quality of HRSC DTM products, it is necessary to establish accurate mapping relationships between tie points in stereo imagery. After extracting and selecting tie points from the stereo imagery through a series of steps, including point matching and filtering, a uniformly distributed set of tie points was obtained. Our matching approach first relies on a rigorous geometric localization model, dividing the matching grid based on the image coverage area to narrow down the matching search region. Subsequently, we employ an image pyramid matching strategy, connecting the tie points from coarse to fine resolution Our matching approach. These tie points are then input into the stereo image self-calibration error compensation model (Wang et al., 2012) to achieve internal consistency of the camera system.

The stereo observation was formed at a 37.8° angle between the forward- and backward-viewing cameras (HRSC–S1 and HRSC–S2) of the satellite. Based on the image point coordinates of the tie points and their corresponding exterior orientation elements, the intersection point of two corresponding image rays in space—that is, the ground point coordinates $(X,Y,Z)^T$—can be determined. By substituting these into the geometric calibration model, the constraint equation is constructed as

$$\begin{bmatrix} X' \\ Y' \\ Z' \end{bmatrix} = m \begin{bmatrix} a_1 & a_2 & a_3 \\ b_1 & b_2 & b_3 \\ c_1 & c_2 & c_3 \end{bmatrix} R_{\text{Camera}} \begin{bmatrix} m_0 + m_1 s + m_2 s^2 \\ n_0 + n_1 s + n_2 s^2 \\ 1 \end{bmatrix} \tag{4}$$

where

$$\begin{bmatrix} X' \\ Y' \\ Z' \end{bmatrix} = \left(R_{J2000}^{\text{Mars}} R_{\text{MEX}}^{J2000} \right)^{-1} \left(\begin{bmatrix} X \\ Y \\ Z \end{bmatrix} - R_{J2000}^{\text{Mars}} \begin{bmatrix} X_S \\ Y_S \\ Z_S \end{bmatrix} \right) = \begin{bmatrix} r_0 & r_3 & r_6 \\ r_1 & r_4 & r_7 \\ r_2 & r_5 & r_8 \end{bmatrix} \begin{bmatrix} X - X'_S \\ Y - Y'_S \\ Z - Z'_S \end{bmatrix} \tag{5}$$

$$R_u(\varphi, \omega, \kappa) = R_\varphi R_\omega R_\kappa = \begin{bmatrix} a_1 & a_2 & a_3 \\ b_1 & b_2 & b_3 \\ c_1 & c_2 & c_3 \end{bmatrix} \tag{6}$$

Establishing the observation equation as follows

$$V = \begin{bmatrix} V_x \\ V_y \end{bmatrix} = \begin{bmatrix} \frac{(\cos\varphi\cos\kappa + \sin\varphi\sin\omega\sin\kappa)X' + \cos\omega\sin\kappa Y' + (\cos\varphi\sin\omega\sin\kappa - \sin\varphi\cos\kappa)Z'}{\sin\varphi\cos\omega X' - \sin\omega Y' + \cos\varphi\cos\omega Z'} - \frac{X_{\text{mex}}}{Z_{\text{mex}}} \\ \frac{(\sin\varphi\sin\omega\cos\kappa - \cos\varphi\sin\kappa)X' + \cos\omega\cos\kappa Y' + (\sin\varphi\sin\kappa + \cos\varphi\sin\omega\cos\kappa)Z'}{\sin\varphi\cos\omega X' - \sin\omega Y' + \cos\varphi\cos\omega Z'} - \frac{Y_{\text{mex}}}{Z_{\text{mex}}} \end{bmatrix} \tag{7}$$

where

$$\begin{bmatrix} X_{\text{mex}} \\ Y_{\text{mex}} \\ Z_{\text{mex}} \end{bmatrix} = R_{\text{Camera}} \begin{bmatrix} m_0 + m_1 s + m_2 s^2 \\ n_0 + n_1 s + n_2 s^2 \\ 1 \end{bmatrix} \tag{8}$$

Taking external calibration as an example, both the object point coordinates $(X, Y, Z)^T$ and exterior orientation elements $R_u(\varphi, \omega, \kappa)$ are optimized and expanded using the Taylor series,

$$V_x = (V_x^0) + \frac{\partial V_x}{\partial X} dX + \frac{\partial V_x}{\partial Y} dY + \frac{\partial V_x}{\partial Z} dZ + \frac{\partial V_x}{\partial \varphi} d\varphi + \frac{\partial V_x}{\partial \omega} d\omega + \frac{\partial V_x}{\partial \kappa} d\kappa$$
$$V_y = (V_y^0) + \frac{\partial V_y}{\partial X} dX + \frac{\partial V_y}{\partial Y} dY + \frac{\partial V_y}{\partial Z} dZ + \frac{\partial V_y}{\partial \varphi} d\varphi + \frac{\partial V_y}{\partial \omega} d\omega + \frac{\partial V_y}{\partial \kappa} d\kappa \tag{9}$$

The next step is to extend it to establish the error equation for the jth tie point in the ith stereo image,

$$V_j^i = A_j^i x^i + B_j^i t_j - l_j^i \tag{10}$$

where $x^i = \begin{bmatrix} d\varphi & d\omega & d\kappa \end{bmatrix}^T$ represents the correction of the exterior orientation parameters for the ith image, and $t_j = \begin{bmatrix} dX & dY & dZ \end{bmatrix}^T$ represents the correction of the object point coordinates for the jth tie point.

$$A_j^i = \begin{bmatrix} \frac{\partial V_x}{\partial \varphi} & \frac{\partial V_x}{\partial \omega} & \frac{\partial V_x}{\partial \kappa} \\ \frac{\partial V_y}{\partial \varphi} & \frac{\partial V_y}{\partial \omega} & \frac{\partial V_y}{\partial \kappa} \end{bmatrix} = \begin{bmatrix} \frac{\frac{\partial XX}{\partial \varphi} ZZ - \frac{\partial ZZ}{\partial \varphi} XX}{ZZ^2} & \frac{\frac{\partial XX}{\partial \omega} ZZ - \frac{\partial ZZ}{\partial \omega} XX}{ZZ^2} & \frac{\frac{\partial XX}{\partial \kappa} ZZ - \frac{\partial ZZ}{\partial \kappa} XX}{ZZ^2} \\ \frac{\frac{\partial YY}{\partial \varphi} ZZ - \frac{\partial ZZ}{\partial \varphi} YY}{ZZ^2} & \frac{\frac{\partial YY}{\partial \omega} ZZ - \frac{\partial ZZ}{\partial \omega} YY}{ZZ^2} & \frac{\frac{\partial YY}{\partial \kappa} ZZ - \frac{\partial ZZ}{\partial \kappa} YY}{ZZ^2} \end{bmatrix}$$

$$B_j^i = \begin{bmatrix} \frac{\partial V_x}{\partial X} & \frac{\partial V_x}{\partial Y} & \frac{\partial V_x}{\partial Z} \\ \frac{\partial V_y}{\partial X} & \frac{\partial V_y}{\partial Y} & \frac{\partial V_y}{\partial Z} \end{bmatrix} = \begin{bmatrix} \frac{\frac{\partial XX}{\partial X} ZZ - \frac{\partial ZZ}{\partial X} XX}{ZZ^2} & \frac{\frac{\partial XX}{\partial Y} ZZ - \frac{\partial ZZ}{\partial Y} XX}{ZZ^2} & \frac{\frac{\partial XX}{\partial Z} ZZ - \frac{\partial ZZ}{\partial Z} XX}{ZZ^2} \\ \frac{\frac{\partial YY}{\partial X} ZZ - \frac{\partial ZZ}{\partial X} YY}{ZZ^2} & \frac{\frac{\partial YY}{\partial Y} ZZ - \frac{\partial ZZ}{\partial Y} YY}{ZZ^2} & \frac{\frac{\partial YY}{\partial Z} ZZ - \frac{\partial ZZ}{\partial Z} YY}{ZZ^2} \end{bmatrix}$$

represents the coefficient matrices for the correction of exterior orientation elements and object point coordinates, respectively; $l_j^i = \begin{bmatrix} -V_x & -V_y \end{bmatrix}^T$ indicates the pointing residual of the jth tie point in the ith image determined from the initial value of the observation,

where

$$\begin{bmatrix} XX \\ YY \\ ZZ \end{bmatrix} = \begin{bmatrix} a_1 X' + b_1 Y' + c_1 Z' \\ a_2 X' + b_2 Y' + c_2 Z' \\ a_3 X' + b_3 Y' + c_3 Z' \end{bmatrix} \tag{11}$$

The self-calibration process based on tie points involves two images and an error equation is established for each of the m tie points in a stereo image,
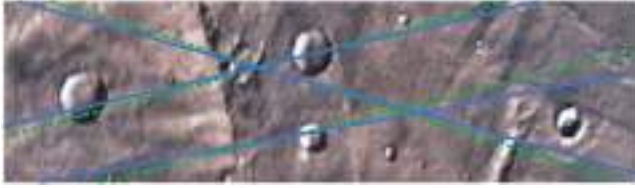
Figure 3. Comparison schematic diagram of the distribution of laser footprints and laser strip projections in an HRSC DTM product after self-calibration based of tie points. Solid lines represent the distribution of laser footprints; dashed lines indicate the projection of the laser strip in the HRSC DTM product.

$$
\begin{aligned}
v_1^{(1)} &= A_1^{(1)} x^{(1)} + B_1^{(1)} t_1 - l_1^{(1)} \\
v_1^{(2)} &= A_1^{(2)} x^{(2)} + B_1^{(2)} t_1 - l_1^{(2)} \\
&\vdots \\
v_m^{(1)} &= A_m^{(1)} x^{(1)} + B_m^{(1)} t_m - l_m^{(1)} \\
v_m^{(2)} &= A_m^{(2)} x^{(2)} + B_m^{(2)} t_m - l_m^{(2)}
\end{aligned}
\tag{12}
$$

To establish the normal equation

$$
\begin{bmatrix} U & W \\ W^T & V \end{bmatrix} \begin{bmatrix} x \\ t \end{bmatrix} = \begin{bmatrix} l_x \\ l_t \end{bmatrix}
\tag{13}
$$

where

$$
\begin{aligned}
U &= A^T PA, V = B^T PB, W = A^T PB \\
l_x &= A^T Pl, l_t = B^T Pl
\end{aligned}
\tag{14}
$$

The matrices U and V are block diagonal matrices. The block Gaussian elimination method is utilized to sequentially solve for the correction vector of ground point coordinates and the exterior orientation elements,

$$
\begin{aligned}
(U - WV^{-1}W^T)x &= l_x - WV^{-1}l_t \\
Vt &= l_t - W^T x
\end{aligned}
\tag{15}
$$

The object point coordinates and exterior orientation elements were updated by solving the correction vector. Similarly, the interior orientation elements were adjusted.

2.2.2. MOLA Matching Unit Construction Algorithm

After performing self-calibration based on multi-view stereo image tie points, which ensures the internal consistency of the camera positioning model, the pitch and yaw angles of the camera during flight were recovered effectively through the offset matrix. However, the orbit bias, drift per line, and roll angle error cannot be eliminated by relying on a single-strip self-calibration algorithm. Orbit bias and attitude roll angle errors, in accordance with the propagation of imaging errors, can result in a systematic offset in the ground point coordinates, whereas the cumulative drift error in the orbit can lead to accumulated bias in the ground point coordinates along the imaging direction. This discrepancy in the positioning accuracy across various locations in the HRSC DTM products is shown in Figure 3.

As the positioning offset direction and magnitude vary across different locations in the image, a direct calculation of the offset between the entire image and the laser strip is not possible. As a result, the laser strip was divided into several sections based on the geographic location. The maximum number of laser points for each section was limited to ensure that the offset direction and magnitude between the laser data in the local area and the corresponding HRSC DTM at the same position were consistent:

$$
N_{\text{laser}} = \frac{R_{\text{DTM}} R_{\text{img}}}{D_{\text{img}} F_{\text{laser}}}
\tag{16}
$$

where N_{laser} represents the maximum number of laser points in each segment after laser strip segmentation, R_{DTM} is the resolution of the HRSC DTM, R_{img} is the resolution of the HRSC image, D_{img} is the drift per line in the measurement error of the satellite orbit position, and F_{laser} indicates the spacing between consecutive laser footprints.

Considering that the similarity of terrain relief between the laser strip and HRSC DTM needs to be calculated subsequently, the following three conditions must be met when selecting the laser strip point set:
(a) Clear terrain undulation within the laser footprint area;
(b) Elevation continuity in the laser footprint point set;
(c) Consistent offset direction and magnitude between the laser footprint point set and HRSC DTM.
According to Equation 16, to ensure the consistency of offset direction and magnitude for all laser points within a matching unit, it is necessary to limit the number of laser points within the unit. The number of points is influenced by factors such as the laser sampling interval and the drift per line in the measurement error of the
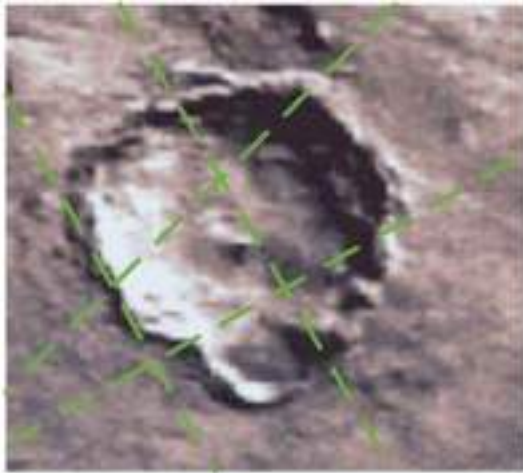
Figure 4. Distribution of local laser footprint point set. Mars Global Surveyor Mars Orbiter Laser Altimeter has multiple observations in locally different directions on the Martian surface.

satellite orbit position. In the case of the MGS laser emission and reception results, there are multiple laser measurements from different observation angles within localized regions on the Martian surface (Figure 4). Additionally, experimental findings indicate that relying solely on the best-fit translation of a single laser profile with the HRSC DTM does not yield significant results. Consequently, a robust laser matching unit is devised by considering the clustering of measurement results from multiple laser strips.

$$R = \frac{\max\limits_{k}\|x_i - c_i\|}{\min\limits_{k}\|c_i - c_j\|}$$

$$\arg\min_{c} J(c) \Rightarrow \arg\min_{c} \sum_{i=1}^{k} \|x_i - c_i\|_2^2 \tag{17}$$

where k denotes the number of clusters, x_i represents the laser points within the ith cluster, c_i, c_j denote the centroids of the ith and jth clusters, respectively, R represents the ratio of the maximum distance from a laser point to its corresponding centroid to the minimum distance between centroids, and the number of clusters is dynamically adjusted based on this ratio. This ensured that each matching unit after clustering contained multiple laser strips in different directions. Multiple elevation curves were fitted and used to create more robust matching units.

2.2.3. Measurement of Terrain Similarity

Owing to the small difference in the geometric positioning error caused by spacecraft roll angle errors in different camera fields of view, the self-calibration algorithm based on single-track connection points cannot constrain the spacecraft roll angle errors. The offset matrix in the self-calibration model can only compensate for certain constant offsets through the pitch and yaw angles, resulting in systematic biases in the HRSC DTM positioning results that affect the elevation intersection results of the stereo connection points. Therefore, the method for minimizing the difference in elevation cannot be used directly to determine the optimal offset (Gläser et al., 2013). In this study, both the correlation of the elevation profiles and absolute elevation differences were considered, and the Concordance Correlation Coefficient (Lawrence & Lin, 1989) was used to quantify the similarity between the HRSC DTM elevation profiles and the laser strip.

$$\rho_c = \frac{2\rho\sigma_D\sigma_L}{\sigma_D^2 + \sigma_L^2 + (\mu_D - \mu_L)^2}$$

$$\rho = \frac{\text{cov}(D, L)}{\sigma_D\sigma_L} \tag{18}$$

where μ_D and μ_L are the means for the elevation values of the corresponding positions of the HRSC DTM and laser points. σ_D^2 and σ_L^2 are the corresponding variances. ρ represents the correlation coefficient between the two variables. Its value ranges from -1 to 1, where a value of 0 indicates no correlation, negative values indicate a negative correlation, and positive values indicate a positive correlation. Where cov is the covariance and σ_D and σ_L are standard deviations.

3. Results and Discussion

3.1. Test Data Sets

In this study, all test data belonged to the standard products of the PDS (Hughes et al., 2014).

3.1.1. MOLA PEDR Data

During the 45-months orbiting of Mars by the MGS spacecraft, over 600 million MOLA laser shots were measured, cross-adjusted, and numbered according to the satellite orbit, resulting in approximately 10,000 laser strips. The elevation accuracy of the laser points was approximately 1.8 m, with a planimetric accuracy of approximately 100 m (Neumann et al., 2001; Smith et al., 2001). The flight trajectory began near the equator and moved toward

Table 3
Parameters of Stereo Image Data

Image type	Orbit number	Imaging time	Maximum resolution (m/pixel)	Swath width	Center of imaging area
Calibration image	I864	2018.11.29	26.9	83 km × 648 km	(28.40°S, 63.13°W)
Validation image	I818	2018.11.16	27.4	88 km × 837 km	(25.85°S, 45.31°W)
Validation image	I863	2018.11.29	28.3	103 km × 741 km	(30.58°S, 37.91°E)
Validation image	I977	2019.01.01	27.2	85 km × 563 km	(51.09°S, 83.93°W)

the Southern Hemisphere, arriving at the South Pole, and then continued to the Northern Hemisphere, arriving at the North Pole. The spacecraft then continued to move toward the Equator, completing one full loop around the planet. The satellite was operated at an altitude of approximately 400 km with a laser beam diameter of approximately 168 m and footprint spacing of approximately 300 m. The interval between adjacent orbits is related to the latitude of the laser point, with the maximum spacing occurring at the equator.

3.1.2. HRSC Stereo Image Data

The experimental images belonged to the MEX mission Level 2 data products, which were compiled and released by the PDS. These products have undergone data decompression and radiometric calibration processing, and are accompanied by satellite flight auxiliary data published by the Navigation Ancillary Information Facility of NASA. These were intended to observe the surface features of Mars. Four sets of stereo images captured by HRSC–S1 and HRSC–S2 were selected for the end of 2018 (Table 3). These images were acquired from different orbits and were separated by approximately 2 months between the acquisition of the first and last images. One image was selected as the calibration image, and the other three images were used as validation images to test the effectiveness of the system error elimination.

3.2. Production of HRSC Image GCPs

This section presents the experimental results of each stage in the production of the HRSC Image GCPs using the stereo image data of the calibration image with orbit number I864 as an example.

3.2.1. MOLA Matching Unit

According to the design of the MGS orbit, there was a systematic shift in the latitude coverage of adjacent laser stripes in the MOLA data. By combining the geographic coverage of the laser data in the initial orbit, the number of laser stripes that overlap geographically with the HRSC DTM can be predicted. Taking orbit number I864 as an example (Figure 5), 126 laser stripes in the MOLA PEDR data set were searched and found to overlap with the DTM, containing 125,749 laser points.

The overlapping laser footprints in the MOLA PEDR data were segmented, filtered, and clustered using the previously introduced robust matching unit strategy, as shown in Figure 6. The red laser point set in the figure represents the laser matching unit processed for elevation curve matching. The segmentation strategy (Equation 14) was used to group the laser points into sets of up to 15. After terrain slope filtering, the number of laser points retained (>10,000) was approximately one-tenth that of the original laser point set. By combining the results with the HRSC DTM, it was observed that the selected laser points were mainly distributed in regions

Figure 5. Distribution of MOLA footprints within the overlap range of HRSC DTM in the orbit I864 stereo image. Red lines indicates the 126 laser strips, and the background map is the HRSC DTM product.
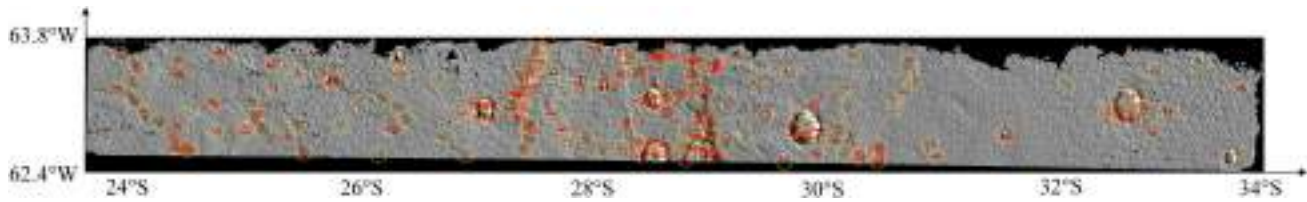
Figure 6. Mars Orbiter Laser Altimeter (MOLA) matching unit (select and group laser footprints from MOLA PEDR data for elevation curve matching). Yellow circles represents the clustering centers of the laser points.

with significant terrain undulations such as impact craters and canyons. The clustering algorithm designed in this study was used to divide the laser points into 150 clusters based on their spatial positions. Each cluster can extract several laser elevation curves to obtain robust laser matching units.

3.2.2. Elevation Consistency

The elevation consistency correlation coefficients corresponding to different translation positions within the HRSC DTM search grid are plotted in Figure 7. Eight sets of laser point clusters were randomly selected from the clustering results (where "index" represents the cluster number). The area of high consistency (i.e., bright yellow spots) within the search grid gradually converges to a point, indicating the highest fit between the laser elevation curve and the DTM elevation profile at this location. This point does not lie at the center of the search grid, indicating that there was a bias in the initial positioning of the satellite. Therefore, the DTM obtained under this positioning accuracy state did not achieve the highest consistency with the laser elevation curve at the corresponding location.

To observe the matching effect of the elevation curve more intuitively, the DTM profile and laser strip elevation curve before and after translation were compared using the same eight sets of clustering results as examples (Figure 8). The number of points in each set of clustered point groups (horizontal axis) was not fixed, with more points indicating a greater number of retained laser points in that area. The curve of elevation corresponding to point number (vertical axis) was formed by combining discrete points. From the three elevation curves (laser elevation, elevation curve obtained by projecting laser points onto the HRSC DTM using the camera positioning
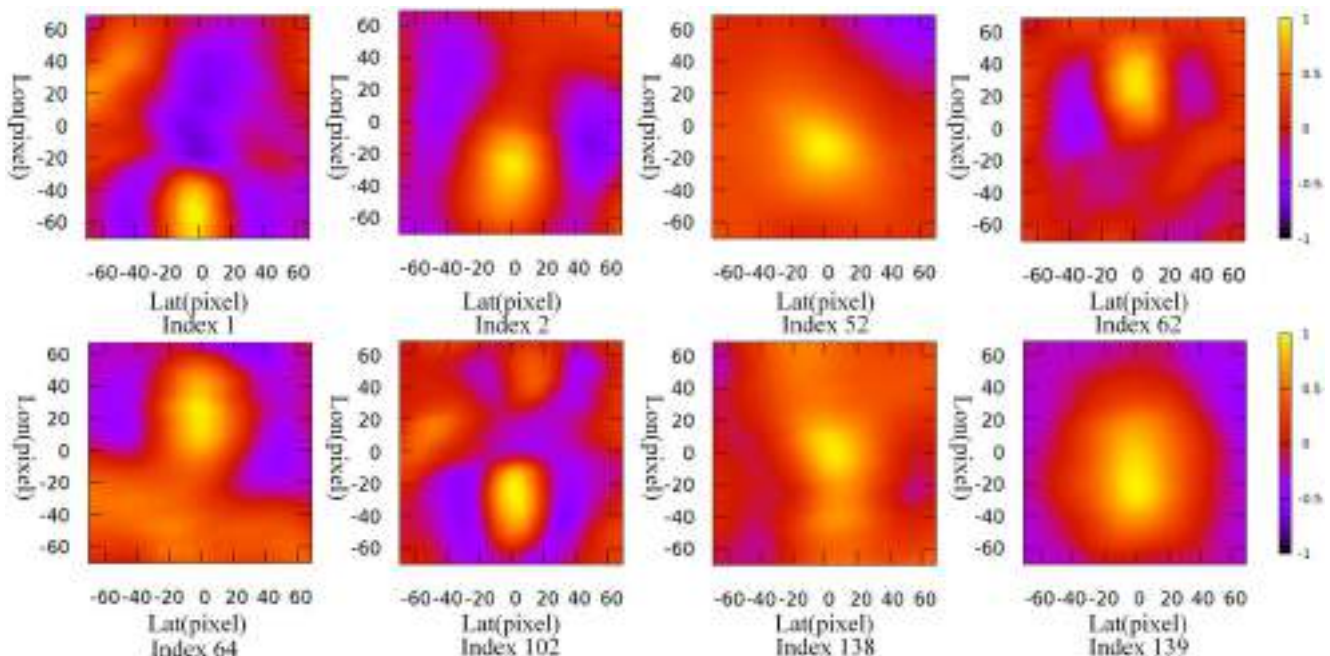

Figure 7. Elevation consistency coefficients corresponding to each translation distance within the search grid. Warm colors represent higher consistency, while cool colors represent lower consistency.
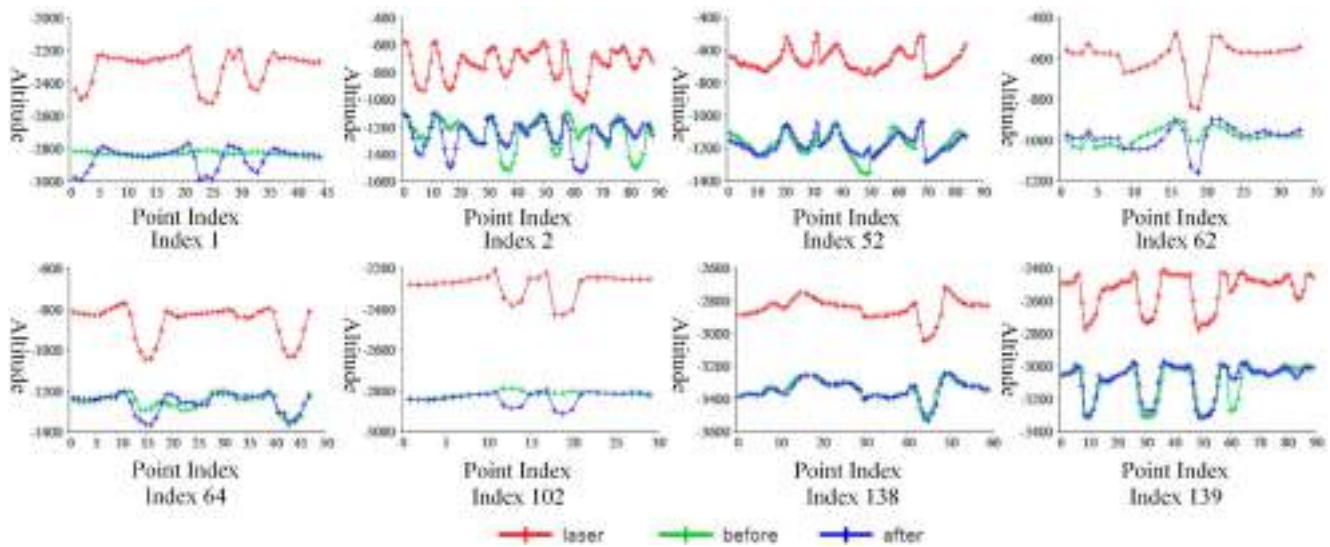
Figure 8. Consistency in elevation fluctuations between HRSC DTM profiles and the laser strip before and after translation. The red curve represents the laser elevation curve, the green curve represents the elevation curve obtained by projecting the laser points onto the HRSC DTM using the camera positioning model, and the purple line represents the curve with the highest fit to the laser elevation curve after elevation consistency alignment.

model, and curve with the highest fit to the laser elevation curve after elevation consistency alignment) and their consistency correlation coefficients (Table 4), it can be observed that the elevation curve of the DTM profile after translation was significantly improved in terms of consistency with the laser elevation curve (correlation coefficients > 0.9). However, although the elevation curves of the DTM profile and laser elevation curve are generally consistent, there is a clear systematic bias between them, which is due to the fact that the connection points only correct the internal consistency accuracy of the satellite, and cannot compensate for the absolute positioning accuracy of the satellite. Therefore, laser control points must be generated during this step.

3.3. Geometric Calibration Accuracy

3.3.1. Calibration Image

As shown in Table 5, prior to calculating the camera calibration parameters, 206 tie points and 476 MOLA GCPs were extracted from the stereo image of orbit I864 using the algorithm described above. The root mean square errors (RMSEs) of the re-projection of the tie points in the S1 and S2 camera positioning models before calibration were 11.21 and 12.11 pixels, respectively. The errors were primarily distributed across the flying direction. The positional accuracies of the S1 and S2 cameras in the horizontal plane, as assessed by comparison with the ground coordinates of the MOLA GCPs, were 682.68 m (25.1 pixels) and 1,049.46 m (36.2 pixels), respectively. The accuracy of the elevation of the stereo intersection point was 507.21 m. After applying a geometric calibration model to compensate for the interior and exterior orientation elements of the camera, both the internal consistency and absolute positioning accuracy of the camera were significantly improved. The RMSEs of the re-projection of tie points in the S1 and S2 camera positioning models after calibration were 0.28 and 0.30 pixels, respectively. The positional accuracy of the S1 and S2 camera in the horizontal plane was 145.31 m (5.6 pixels) and 144.61 m (5.2 pixels), respectively, and the accuracy of the elevation of the stereo intersection point was 63.98 m (2.3 pixels).

Further analysis of the calibration accuracy of the calibration image for orbit I864 reveals that the internal distortion of the HRSC–S1 and HRSC–S2 stereo cameras is superior to one pixel in both the along-track and

Table 4
Consistency Coefficient of the Elevation Profile Before and After Translation

Index	1	2	52	62	64	102	138	139
Before CCC	− 0.645	0.312	0.794	0.297	0.719	− 0.268	0.911	0.866
After CCC	0.971	0.951	0.971	0.925	0.943998	0.976	0.945	0.973

Table 5
Positioning Accuracy of the Orbit I864 Image Before and After Calibration

Calibration	Camera number	Internal consistency			Absolute accuracy		
		Across-track (pixel)	Along-track (pixel)	Focal plane (pixel)	Horizontal plane (pixel)	Horizontal plane (m)	Elevation (m)
Before	S1	11.190	0.607	11.207	25.077	682.675	507.214
	S2	12.081	0.814	12.108	36.195	1,049.461	
After	S1	0.275	0.013	0.276	5.650	145.314	63.978
	S2	0.298	0.017	0.299	5.254	144.605	

across-track directions, indicating that their internal consistency has reached the level of Earth observation satellites. The absolute positioning accuracy has an elevation accuracy of approximately two pixels, whereas the camera plane positioning accuracy can only reach approximately 5 pixels, which is lower than the calibration results of general Earth observation satellites. This is attributed to the use of MOLA GCPs to quantitatively assess the absolute positioning accuracy of the camera. However, the laser data can only achieve a planar accuracy on the order of hundreds of meters (equal to the calibration accuracy). Therefore, the calibration results of the experiment are acceptable for extra-terrestrial calibration tasks that lack real ground control point data.

The generated HRSC DTM profiles before and after calibration were extracted and compared with the laser elevation profile (MOLA orbit number AP10228) to verify the absolute positioning accuracy of the post-calibration model, as shown in Figure 9. It should be noted that to enable the stereo intersection of the corresponding image points, the HRSC DTM before and after calibration were both subjected to adjustments based on the geometric calibration model of the tie points. From Figure 9, there is a systematic deviation of more than 400 m between the DTM elevation curve and the laser elevation curve before calibration. However, after calibration, the DTM elevation curve almost completely overlaps the laser elevation curve, demonstrating a significant improvement in the absolute positioning accuracy of the camera. Furthermore, there are two noticeable concavities in the laser elevation curve at positions labeled (a) and (b) in the figure, which correspond to impact craters. A comparison of the laser footprint positions before and after calibration revealed that before calibration, the laser footprints at position (a) were located at the edge of the impact crater, and at position (b), the laser footprints did not pass
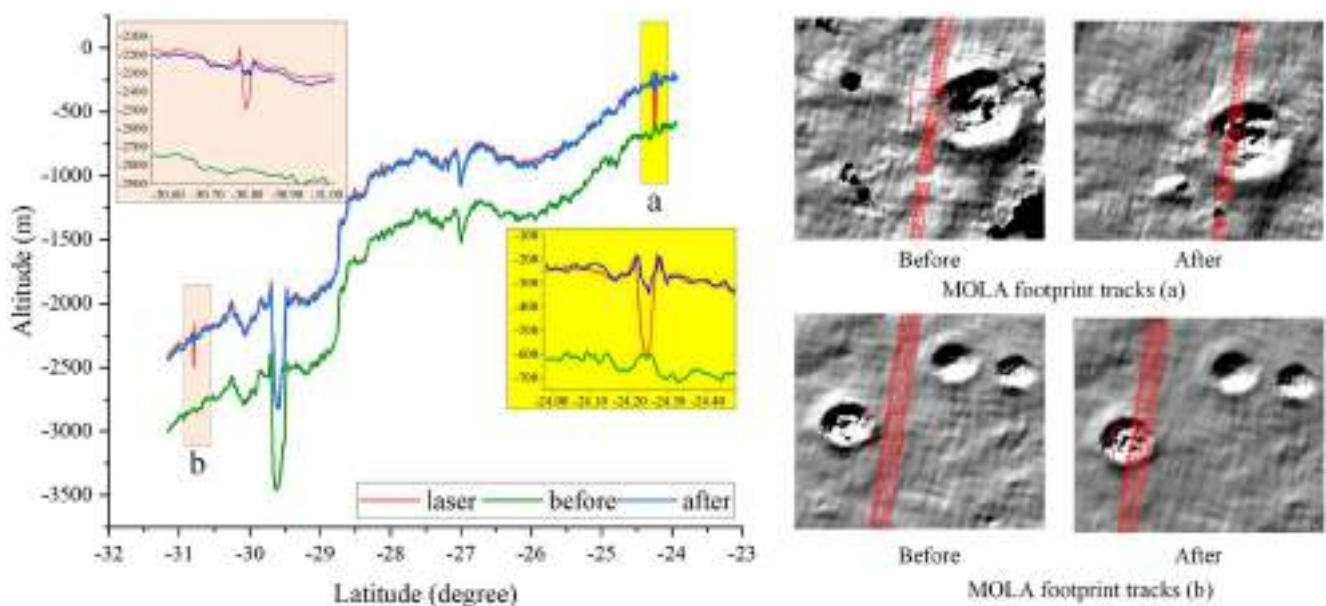

Figure 9. Comparison diagram of the elevation profile curves between HRSC DTM and laser strip (orbit number AP10228) before and after calibration. The figure on the left shows the latitude coordinates of Mars on the horizontal axis, with negative values representing the Southern Hemisphere and the elevation value corresponding to each point on the vertical axis. The red line represents the laser elevation curve and the green and blue lines represent the elevation curves extracted from the DTM produced before and after calibration, respectively.

Table 6
Direct Geolocation Accuracy of Validation Images (Camera Internal Accuracy and Absolute Accuracy)

Image number	Camera number	Internal consistency			Absolute accuracy		
		Across-track (pixel)	Along-track (pixel)	Focal plane (pixel)	Horizontal plane (pixel)	Horizontal plane (m)	Elevation (m)
I818	S1	10.294	0.563	10.310	24.252	684.161	477.180
	S2	10.600	0.657	10.620	30.791	900.743	
I863	S1	10.495	0.624	10.513	24.553	704.422	471.415
	S2	10.087	0.576	10.104	33.027	911.537	
I977	S1	6.448	0.248	6.453	21.709	602.496	682.407
	S2	6.451	0.272	6.457	29.345	803.388	

through the impact crater area. After calibration, the laser footprints at positions (a) and (b) were projected onto the impact crater area, demonstrating an effective improvement in planimetric positioning accuracy. Furthermore, there was a consistent trend of elevation fluctuation between the elevation profile and laser elevation curve, both of which exhibited significant concavities. Nevertheless, owing to the effects of line-of-sight obstruction and DTM construction accuracy, it was difficult to accurately measure the degree of elevation drop within the impact crater, resulting in varying elevation descent values.

3.3.2. Validation Image

The camera calibration parameters obtained by processing the stereo images from orbit I864 were added directly to the geometric localization model of the other three validation images. By comparing the changes in the positioning accuracy of the three validation images before and after adding the calibration parameters (Tables 6 and 7), both the internal consistency and absolute positioning accuracy of the camera improved significantly.

The direct geolocation accuracy of the three validation images showed that the internal distortions of the camera exceeded 6 pixels, and the re-projection error was mainly distributed along-track direction. After adding the calibration parameters, the RMSE of the re-projected stereo matching points in the S1 and S2 camera models of validation images I818 and I863 reached the sub-pixel level, and that of validation image I977 was close to 1 pixel.

By comparing the geographic coordinates of the MOLA GCPs extracted from the three verification images, the planar positioning accuracy of HRSC-S1 and HRSC-S2 improved from approximately 800 m (26.5 pixels) to approximately 250 m (8.3 pixels) after adding the calibration parameters. The elevation accuracy of the stereo intersection in verification images I818 and I863 improved from approximately 470 m (15.6 pixels) to within 100 m (3 pixels). However, owing to the lower internal consistency accuracy of the I977 images, the elevation accuracy of the stereo intersection improved from 682.41 m (22.7 pixels) to 256.64 m (8.5 pixels), which was still lower than that of the first two images.

Further analysis of the slightly lower accuracy of the I977 validation image compared with the other two images suggests that the reason may be the longer time elapsed between the acquisition of the I977 image and the I864

Table 7
Positioning Accuracy of the Validation Image After Adding Calibration Parameters

Image number	Camera number	Internal consistency			Absolute accuracy		
		Across-track (pixel)	Along-track (pixel)	Focal plane (pixel)	Horizontal plane (pixel)	Horizontal plane (m)	Elevation (m)
I818	S1	0.328	0.023	0.329	7.894	217.017	66.032
	S2	0.333	0.027	0.334	8.349	235.313	
I863	S1	0.573	0.037	0.574	9.917	273.349	80.013
	S2	0.543	0.032	0.544	10.952	301.776	
I977	S1	1.029	0.062	1.030	6.681	178.716	256.643
	S2	1.016	0.078	1.019	10.469	286.364	

calibration image. Although the calibration parameters can still significantly improve the camera positioning accuracy, the effect of the improvement gradually decreases over time owing to the influence of the spatial environment. Therefore, periodic calibration tasks are necessary to maintain in-orbit satellite operation.

4. Conclusions

Based on the parameters and imaging method of the high-resolution stereo camera sensor carried by the MEX orbiter, this study combined satellite flight assistance data published by NAIF to construct a rigorous line array push-broom geometric model of the HRSC camera. Considering the imaging error and its impact on the positioning accuracy, pointing angles and bias matrices were introduced to compensate for the measurement errors in the internal and external orientation elements of the camera, and a rigorous imaging geometry model was constructed for geometric calibration. This paper also proposes a method for extracting Martian ground control points. The method accurately identifies the image coordinates of the laser points by matching the elevation curve between the laser strip and the HRSC DTM profile. This enables the establishment of planar and elevation control for the image combined with the tie points and a geometric calibration model. This improves the internal consistency and absolute positioning accuracy of the camera and achieves significant results in both the calibration and validation images. The experimental results showed that after calibration, the internal distortion of the HRSC stereo camera was better than that of 1 pixel in both the along-track and across-track directions. The planimetric accuracy of the calibrated images was approximately 140 m (~5 pixels), and the planimetric accuracy of the validation images was better than 300 m (~10 pixels), which is a significant improvement compared with the kilometer-level accuracy achieved by direct positioning. In addition, before and after calibration, the height accuracy of the intersection of homologous points improved significantly from approximately 500 m to within 100 m (~3 pixels), indicating a significant improvement in accuracy.

Compared with the traditional geometric calibration method based on MOLA DTM constraints (Gwinner et al., 2016; Kirk et al., 2020; Michael et al., 2016), which minimizes the distance d defined as the vertical distance between the HRSC point H to the bilinear surface defined by the four points (Heipke et al., 2004), this study developed a MOLA GCPs extraction algorithm that can accurately identify the image coordinates of the laser footprint in the image and provide planar control while establishing elevation constraints. The elevation constraint is not directly calculated based on the vertical distance between the HRSC point and the nearest grid in the DTM. In addition, the calibration model only compensates for systematic errors in the internal and external orientation elements; therefore, the calibration parameters can be added to other experimental images acquired during the same period to quickly improve the direct positioning accuracy of the camera and increase the production efficiency of planetary cartographic products.

Although the experimental results demonstrated that the camera positioning accuracy was significantly improved through the calibration algorithm developed in this study, there were still errors in the absolute positioning accuracy of the planar precision of the calibrated image (~5 pixels) and the validation image (~8 pixels). Considering the planimetric accuracy of MGS MOLA laser points, which is on the order of hundreds of meters, as well as the fact that the height value of MOLA may not necessarily correspond to the central altitude of the illuminated area, and the influence of errors in laser control point extraction, the accuracy achieved is close to the theoretical limit that can be attained under these specific MOLA GCPs conditions.

Data Availability Statement

Data for MOLA PEDR and HRSC images were downloaded using the PDS Geosciences Node Mars Orbital Data Explorer located at https://pds-geosciences.wustl.edu/missions/mep/index.htm (PDS, 2023). The auxiliary data and SPICE Toolkit software can be found at https://naif.jpl.nasa.gov/pub/naif/ (NASA, 2023). Additionally, we have hosted our source code and related information at https://doi.org/10.5281/zenodo.8232176 (NEFUL-IDA, 2023), with continuous updates and maintenance as our research progresses.

References

Acton, C., Bachman, N., Semenov, B., & Wright, E. (2016). SPICE tools supporting planetary remote sensing. In *23rd congress of the international society-for-photogrammetry-and-remote-sensing (ISPRS)* (pp. 357–359). https://doi.org/10.5194/isprsarchives-XLI-B4-357-2016

Albertz, J., Attwenger, M., Barrett, J. M., Casley, S., Dorninger, P., Dorrer, E., et al. (2005). HRSC on Mars Express–photogrammetric and cartographic research. *Photogrammetric Engineering & Remote Sensing*, *71*(10), 1153–1166. https://doi.org/10.14358/PERS.71.10.1153

Chicarro, A., Martin, P., & Trautner, R. (2004). The Mars Express mission: An overview. *Mars Express: The Scientific Payload*, *1240*, 3–13.

Ebner, H., & Müller, F. (1987). Processing of digital three-line imagery using a generalized model for combined point determination. *Photogrammetria*, *41*(3), 173–182. https://doi.org/10.1016/0031-8663(87)90031-7

Ebner, H., & Ohlhof, T. (1994). Utilization of ground control points for image orientation without point identification in image space. In *ISPRS commission III symposium: Spatial information from digital photogrammetry and computer vision* (pp. 206–211). International Society for Optics and Photonics.

Ebner, H., & Strunz, G. (1988). Combined point determination using digital terrain models as control information. *International Archives of Photogrammetry and Remote Sensing*, *27*, 578–587.

Edmundson, K. L., Cook, D. A., Thomas, O. H., Archinal, B. A., & Kirk, R. L. (2012). Jigsaw: The ISIS3 bundle adjustment for extraterrestrial photogrammetry. In *ISPRS annals of the photogrammetry, remote sensing and spatial information sciences XXII ISPRS congress, 1–4* (pp. 203–208). https://doi.org/10.5194/isprsannals-I-4-203-2012

Gläser, P., Haase, I., Oberst, J., & Neumann, G. A. (2013). Co-registration of laser altimeter tracks with digital terrain models and applications in planetary science. *Planetary and Space Science*, *89*, 111–117. https://doi.org/10.1016/j.pss.2013.09.012

Granshaw, S. I. (2020). Photogrammetric terminology. *Photogrammetric Record*, *35*(170), 143–288. https://doi.org/10.1111/phor.12314

Gwinner, K., Jaumann, R., Hauber, E., Hoffmann, H., Heipke, C., Oberst, J., et al. (2016). The high resolution stereo camera (HRSC) of Mars Express and its approach to science analysis and mapping for Mars and its satellites. *Planetary and Space Science*, *126*, 93–138. https://doi.org/10.1016/j.pss.2016.02.014

Heipke, C., Ebner, H., Schmidt, R., Spiegel, M., Brand, R., Baumgartner, A., & Neukum, G. (2004). Camera orientation of Mars Express using DTM information, pattern recognition. In *26th DAGM symposium, Tübingen, Germany, August 30–September 1, 2004* (Vol. 26, pp. 544–552). Springer.

Hughes, J. S., Crichton, D., Hardman, S., Law, E., Joyner, R., & Ramirez, P. (2014). PDS4: A model-driven planetary science data architecture for long-term preservation. In *Paper presented at 30th international conference on data engineering workshops* (Vol. 2014, pp. 134–141). IEEE Publications. https://doi.org/10.1109/ICDEW.2014.6818317

Jiang, Y.-H., Zhang, G., Tang, X.-M., Li, D., Huang, W.-C., & Pan, H.-B. (2013). Geometric calibration and accuracy assessment of ZiYuan-3 multispectral images. *IEEE Transactions on Geoscience and Remote Sensing*, *52*, 4161–4172. https://doi.org/10.1109/TGRS.2013.2280134

Jiang, Y. H., Zhang, G., Tang, X. M., & Zhu, X. Y. (2013). High accuracy geometric calibration of ZY-3 three-line image. *Acta Geodaetica et Cartographica Sinica*, *42*, 523–529.

Kim, J. R., & Muller, J. P. (2007). Geometric ground control of very high resolution imagery using HRSC intersection points and a non-rigorous camera model. In *Paper presented at 38th annual lunar and planetary science conference* (Vol. 1811).

Kirk, R. L., Fergason, R. L., Redding, B., Galuszka, D., Smith, E., Mayer, D., et al. (2020). Evaluating stereo DTM quality at Jezero Crater, Mars with HRSC, CTX, and Hirise images. *The International Archives of the Photogrammetry, Remote Sensing and Spatial Information Sciences*, 1129–1136. https://doi.org/10.5194/isprs-archives-XLIII-B3-2020-1129-2020

Lawrence, I., & Lin, K. (1989). A concordance correlation coefficient to evaluate reproducibility. *Biometrics*, *45*(1), 255–268. https://doi.org/10.2307/2532051

Michael, G. G., Walter, S. H. G., Kneissl, T., Zuschneid, W., Gross, C., McGuire, P. C., et al. (2016). Systematic processing of Mars Express HRSC panchromatic and colour image mosaics: Image equalisation using an external brightness reference. *Planetary and Space Science*, *121*, 18–26. https://doi.org/10.1016/j.pss.2015.12.002

National Aeronautics and Space Administration. (2023). SPICE toolkit (version N66) [Software]. Navigation and Ancillary Information Facility. Retrieved from https://naif.jpl.nasa.gov/naif/toolkit.html

NEFULIDA. (2023). NEFULIDA/Mars: v1.0.0 (v1.0.0) [Software]. Zenodo. https://doi.org/10.5281/zenodo.8232176

Neukum, G., & Jaumann, R., & the HRSC Co-Investigator and Experiment Team. (2004). HRSC: The high resolution stereo camera of Mars Express. *Mars Express: The Scientific Payload*, *1240*, 17–35.

Neumann, G. A., Rowlands, D. D., Lemoine, F. G., Smith, D. E., & Zuber, M. T. (2001). Crossover analysis of Mars orbiter laser altimeter data. *Journal of Geophysical Research*, *106*(E10), 23753–23768. https://doi.org/10.1029/2000JE001381

Planetary Data System. (2023). Mars Express high resolution stereo camera and MOLA PEDR dataset (version PDS4) [Dataset]. PDS Geosciences Node Mars Orbital Data Explorer. Retrieved from https://pds-geosciences.wustl.edu/missions/mep/index.htm

Putri, A. R. D., Sidiropoulos, P., Muller, J. P., Walter, S. H. G., & Michael, G. G. (2019). A new south polar digital terrain model of Mars from the high-resolution stereo camera (HRSC) onboard the ESA Mars Express. *Planetary and Space Science*, *174*, 43–55. https://doi.org/10.1016/j.pss.2019.02.010

Schmidt, R., Spiegel, M., & Heipke, C. (2008). Operational determination of tie points and bundle adjustment of HRSC images of the mars Express Mission. *International Archives of Photogrammetry and Remote Sensing*, *37*(4), 1025–1030.

Scholten, F., Gwinner, K., Roatsch, T., Matz, K.-D., Wählisch, M., Giese, B., et al. (2005). Mars express HRSC data processing—Methods and operational aspects. *Photogrammetric Engineering & Remote Sensing*, *71*(10), 1143–1152. https://doi.org/10.14358/PERS.71.10.1143

Smith, D. E., Zuber, M. T., Frey, H. V., Garvin, J. B., Head, J. W., Muhleman, D. O., et al. (2001). Mars orbiter laser altimeter: Experiment summary after the first year of global mapping of Mars. *Journal of Geophysical Research*, *106*(E10), 23689–23722. https://doi.org/10.1029/2000JE001364

Smith, D. E., Zuber, M. T., Sean, C. S., Phillips, R. J., Head, J. W., Garvin, J. B., et al. (1999). The global topography of Mars and implications for surface evolution. *Science*, *284*(5419), 1495–1503. https://doi.org/10.1126/science.284.5419.1495

Spiegel, M. (2007a). Improvement of interior and exterior orientation of the three line camera HRSC with a simultaneous adjustment. *International Archives of Photogrammetry and Remote Sensing*, *36*, 161–166.

Spiegel, M. (2007b). *Kombinierte Ausgleichung der Mars Express HRSC Zeilenbilddaten und des Mars Global Surveyor MOLA DGM*. Technische Universität München.

Wang, M., Cheng, Y. F., Chang, X. L., Long, X. X., & Li, Q. P. (2017). High accuracy on-orbit geometric calibration of geostationary satellite GF4. *Acta Geodatica et Cartographica Sinica*, *46*, 53–61. https://doi.org/10.11947/j.AGCS.2017.20160300

Wang, T., Zhang, Y. S., Zhang, Y., & Fan, D. Z. (2012). Airborne linear CCD sensor geometric calibration based on self-calibration. *Acta Geodatica et Cartographica Sinica*, *41*, 393–400.

Zhang, G., Jiang, Y., Li, D., Huang, W., Pan, H., Tang, X., & Zhu, X. (2014). In-orbit geometric calibration and validation of ZY-3 linear array sensors. *Photogrammetric Record*, *29*(145), 68–88. https://doi.org/10.1111/phor.12052